Appendix: Spectral Control via Multi-Species Effects in PW-Class Laser-Ion Acceleration

Axel Huebl,[1,2,*] Martin Rehwald,[1,2] Lieselotte Obst-Huebl,[1,2] Tim Ziegler,[1,2] Marco Garten,[1,2] René Widera,[1] Karl Zeil,[1] Thomas E. Cowan,[1,2] Michael Bussmann,[1] Ulrich Schramm,[1,2] and Thomas Kluge[1]

[1] *Helmholtz-Zentrum Dresden - Rossendorf, 01328 Dresden, Germany*
[2] *Technical University Dresden, 01062 Dresden, Germany*

(Dated: March 6, 2019)

Data availability

Simulation input files, in situ analysis output, scripts and analyzed data that support the figures and other findings of this study are available from:

DOI:10.14278/rodare.116
URL: https://doi.org/10.14278/rodare.116

PIConGPU is open source and all versions, including 0.4.3 used in this paper, are available as download and contributable git repository[43, 44].

Additional high-resolution, raw HDF5 files using the openPMD standard (DOI:10.5281/zenodo.1167843) increase simulation output data to 4.7 TByte and are available from the corresponding author upon reasonable request.

Simulation Setup Overview

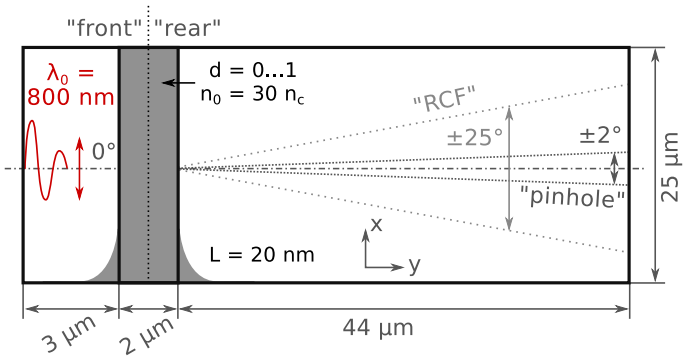

FIG. 4. Simulation setup and used naming conventions. In situ applied particle filters are modeled according to a synthetic RCF stack or pinhole, e.g. in a Thomson parabola. Laser incident angle is zero degrees (from left along y) and polarization is parallel to the simulated plane.

Figure 4 shows the simulation box, with the laser pulse propagating in positive y direction.

The initial density profile is modeled after (all in µm):

$$n_e(y) = 30\,n_c \cdot \begin{cases} \mathrm{e}^{-(y-5)/0.02}, & \text{if } y > 5 \\ 1, & \text{if } 3 < y < 5 \\ \mathrm{e}^{(y-3)/0.02}, & \text{if } y < 3 \end{cases} \tag{4}$$

Numerical particle-in-cell solvers deployed are Yee Maxwell-solver, optimized Esirkepov current deposition (ZigZag path splitting), randomized in-cell starting positions without temperature, 3rd order (piecewise cubic) particle assignment shape, Boris particle pusher, and weighted trilinear force interpolation. Collision operators are neglected.

The 2D simulations' spatial resolution is $\Delta x, \Delta y = 3.33\,\mathrm{nm}$ with $\Delta t = 7.85\,\mathrm{as}$ on a grid of 7488x14720 cells. Equivalently, the central laser wavelength is resolved with 240 cells and the non-relativistic plasma frequency $\omega_\mathrm{p} \cdot \Delta t =$

0.10. Per ion species, 20 particles per cell and one electron particle per ion is initialized as pre-ionized macro-particle distribution. Each simulation computes 0.60 ps interaction time on 16 GPUs (Nvidia P100) within 1:20-1:45 hours.

The laser pulse's peak intensity reaches the target after 8190 steps (64.3 fs). Energy spectra were compared on final, converged results before particles leave the simulation box, at step 90 000, 75 000, 70 000, 60 000 or 45 000, depending on laser intensity.

Simulation and Analytical Results for $a_0 = 8, 23, 30, 42$

The explicit form of the prediction for the heavier species' cutoff energy in eq. (3) is:

$$K_{\mathrm{D}}^{\mathrm{ctf}}(d, T_{\mathrm{e}}) = \frac{m_{\mathrm{D}}}{2} \cdot \left(\sqrt{K_{\mathrm{D}}^{d=1,\mathrm{ctf}} \cdot \frac{2A_{\mathrm{D}}}{m_{\mathrm{D}}}} - (1-d) \cdot \frac{Z_{\mathrm{H}}}{\mathfrak{e} \cdot Z_{\mathrm{D}}} \sqrt{\frac{Z_{\mathrm{H}} k_{\mathrm{B}} T_{\mathrm{e}}}{m_{\mathrm{H}}}} \cdot \left(\frac{\mathfrak{e}^{3\mathfrak{m}_r}}{2^{\mathfrak{m}_r}} \cdot \frac{\tau_{\mathrm{D}}^{2-2\mathfrak{m}_r} - 1}{2 - 2\mathfrak{m}_r} - \frac{\mathfrak{e}^3 \mathfrak{m}_r^2}{2} \cdot \ln(\tau_{\mathrm{D}}) \right) \right)^2 . \quad (5)$$

All quantities are given in SI, $\mathfrak{e}$ is Euler's number, $\mathfrak{m}_r^2 = m_{\mathrm{H}} m_{\mathrm{D}}^{-1}$ and $\tau_{\mathrm{D}} = t \cdot \omega_{\mathrm{p,D}}^{d=1} \approx 1.3 \cdot \tau_{\mathrm{laser}}^{\mathrm{I,FWHM}} \cdot \omega_{\mathrm{p,D}}^{d=1}$ are unitless[1].

Replacing $Z_{\mathrm{D}}, A_{\mathrm{D}}, m_{\mathrm{D}}$ for any other heavy ion species or choosing another "light" ion species for the same quantities in X_{H} variables should hold true and no assumptions over the abundance or ratio between the two are taken into the derivation. Note to readers: previous papers [29, 32] annotated quantities X_{H} for "heavy" and X_{L} for "light" ions. Our choice of H of the light hydrogen (proton) species is the exact opposite. Translating [29, 32] eq. (1) in our nomenclature reads

$$K_{\mathrm{D}}^{\mathrm{ctf}} = Z_{\mathrm{D}} T_{\mathrm{e}} \ln^2 \left[4 Z_{\mathrm{D}} d \sqrt{2 A_{\mathrm{D}} Z_{\mathrm{H}} / A_{\mathrm{H}} Z_{\mathrm{D}}} / (Z_{\mathrm{H}} (d-1) \mathfrak{e}) \right] / 2 \quad (6)$$

$$K_{\mathrm{H}}^{\mathrm{peak}} = Z_{\mathrm{H}} T_{\mathrm{e}} \ln \left[4 Z_{\mathrm{D}} d \sqrt{2 A_{\mathrm{D}} Z_{\mathrm{H}} / A_{\mathrm{H}} Z_{\mathrm{D}}} / (Z_{\mathrm{H}} (d-1) \mathfrak{e}) \right] . \quad (7)$$

In our model, we derive the cutoff energy $K_{\mathrm{D}}^{\mathrm{ctf}}$ of the heavier species. As the lighter species is shifted to higher energies from this spectral position, a peak is observed at $K_{\mathrm{H}}^{\mathrm{peak}}$ for protons. Previous models described this as in eq. (7). This is the grey dotted line in Figures 1 and 5.

Figure 5 provides additional spectra collection for various simulated laser intensities of the main text. Averaged kinetic energies $\langle T_{\mathrm{e}} \rangle$ and $n_{\mathrm{e}}^{\mathrm{rear}}$ are a best-effort to measure in situ from simulation data. Please see assumptions and method in provided scripts. Alternatively, like previous authors one can also just apply a theoretical scaling for the average kinetic energy, such as [8], and approximate $n_{\mathrm{e}}^{\mathrm{rear}} \approx n_0 \cdot \eta$ via the absorption in Figure 6.

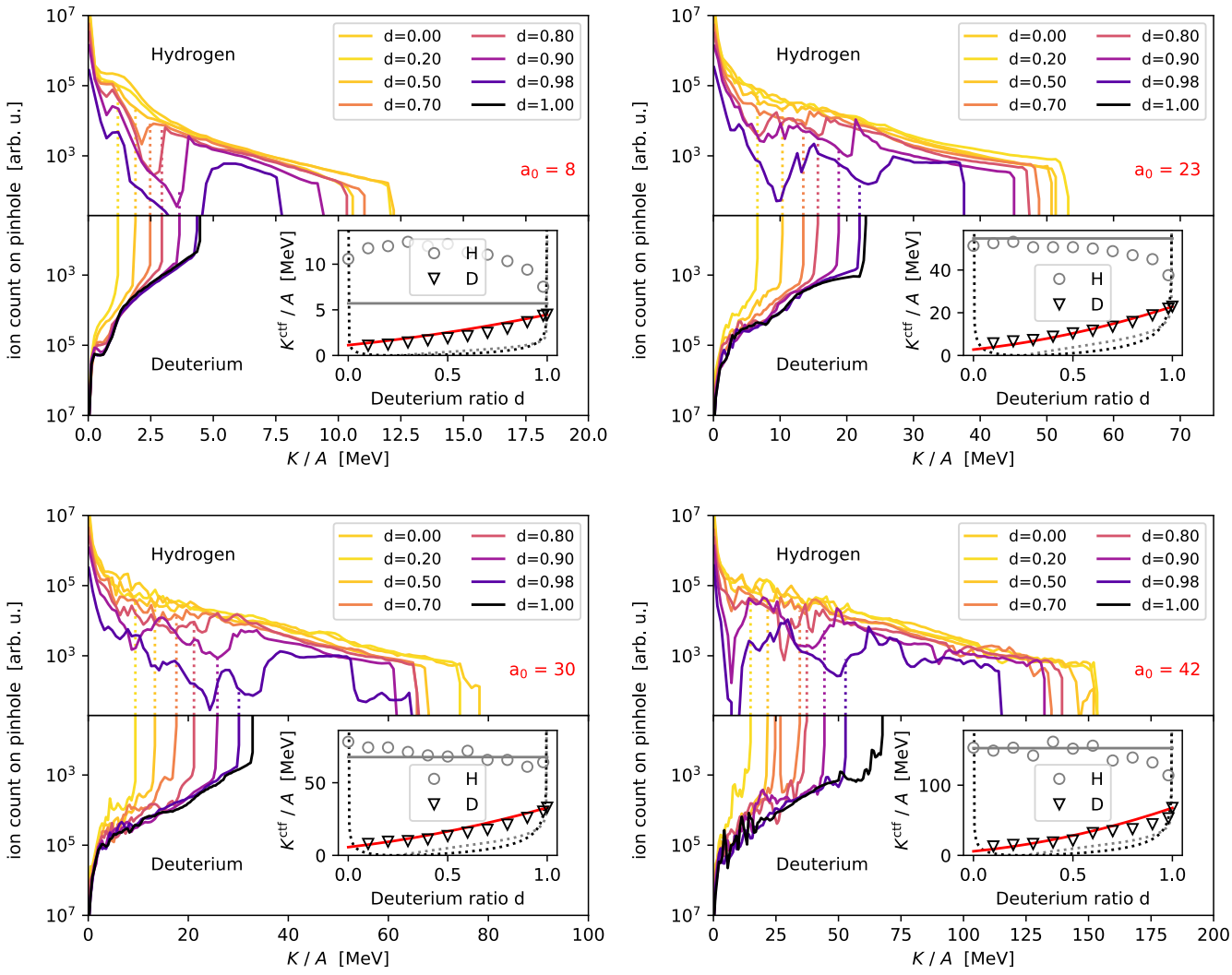

FIG. 5. Deuterium and hydrogen energy spectra for laser strengths parameter $a_0 = 8-42$. Individually shown as in Figure 1 for variations in target Deuterium ratio d. Ions shown for ± 2 degree "pinhole" acceptance. The theoretical prediction from eq. (3) is presented as red solid line and hydrogen cutoff following Mora scaling as grey line [6] for $T_e = (0.35, 3.52, 4.52, 8.64)$ MeV and non-perfect absorption into rear electrons $n_e^{rear} = (0.48, 0.44, 0.40, 0.57) \cdot n_{0,e}$ for $a_0 = (9, 23, 30, 42)$. Dashed lines are previous models ($d \approx 1$) for heavy species cutoff (black) and light species peak (grey) from eqs. (6), (7).

Determination of $\langle T_e \rangle$ and n_e^{rear}

Figure 6 shows the relative ratio of laser energy absorbed by the target.

In order to estimate the average kinetic energy $\langle T_e \rangle$ and n_e^{rear} for electrons in simulations, various methods are used by contemporary literature, yet rarely documented. Either apply one of the theoretical models for $\langle T_e \rangle$, such as [8], and assume the all-target absorption $\eta \approx n_e^{rear}/n_{0,e}$ or try to measure in situ as shown in Figure 7.

In our analysis of electrons in the simulation, we select a spatial region around the laser axis in the second half of the target and measure the prompt, laser-accelerated electrons with relativistic values for γ_e. We measure shortly after the laser peak intensity reaches the target. The resulting average kinetic energy and density is then corrected for the missing low-energy contribution due to our spectral γ_e-cutoff, assuming a Boltzmann distribution, which we verify in electron energy histograms for the assumed "prompt" selection.

We observe derivations from those predictions at $a_0 = 8$ and 42. Comparing theoretical predictions for Hydrogen cutoff energy for $a_0 = 8$, we realize our selection of prompt electrons underestimates the electron density relevant for acceleration of ions. We therefore included a fraction of bulk electrons in this specific measurement in order to

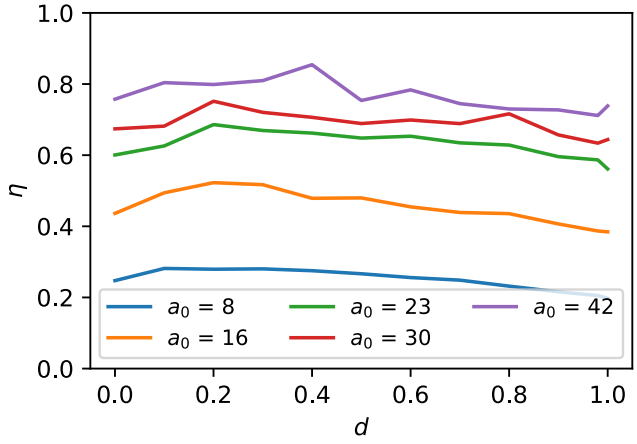

FIG. 6. Energy conversion η from laser energy to kinetic particle energy over laser strength parameter a_0 and relative deuterium content d.

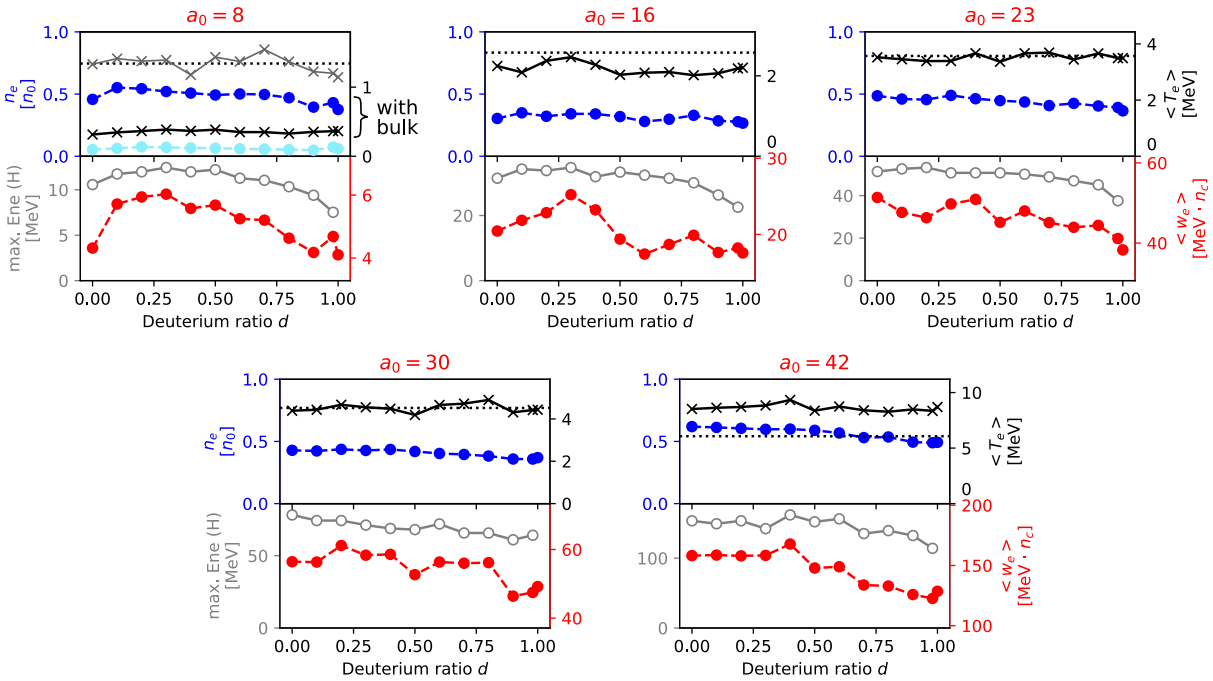

FIG. 7. In situ measured parameters for laser accelerated electrons: density ratio to cold target, average kinetic energy, resulting average energy density versus hydrogen cutoff energy. The black dashed line is the theoretical scaling from [8] eq. (9).

account for re-heating effects and slow expansion, which is influenced by non-prompt electrons at this low intensity. Nevertheless, this method of measurement likely underestimates the average kinetic energy of electrons due to crude averaging of both bulk and prompt electron distributions. Due to burn-through of the target for the $a_0 = 42$ case, the laser can penetrate the target and electrons can co-propagate with its phase, increasing the average electron energy above the case of a solid, reflecting surface and therefore values exceed the dashed black line, showing Ref. [8] eq. (9).

Observing the energy-density of laser accelerated electrons in Figure 7 (red data points), a maximum is achieved for a deuterium ratio of about $d = 20 - 50\,\%$ for $a_0 < 20$. Following [6], this translates into a maximum acceleration field and hence maximum proton energies (grey data points).

We therefore conclude that the deuterium ratio in the target modifies the front side absorption of the laser energy into Debye sheath electrons. Since we do not observe a correlated change in the front side plasma steepness, this

change in absorption is likely due to varied micro-structuring of the surface or other 2D effects.

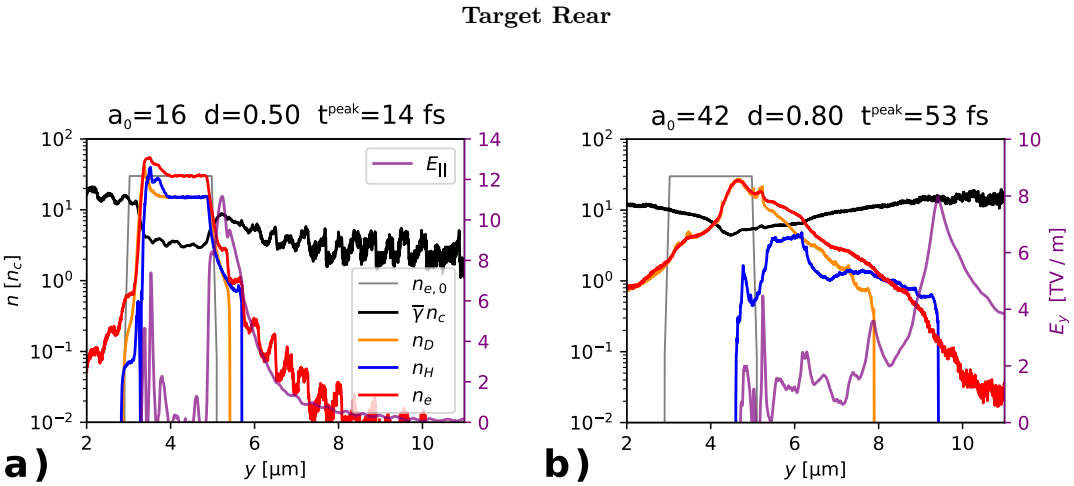

FIG. 8. Lineouts of plasma density and longitudinal electric field an early stage of the acceleration. **a)** $a_0 = 16$ and target deuterium ratio $d = 0.5$. **b)** $a_0 = 42$ and target deuterium ratio $d = 0.8$.

Figure 8a) exemplifies the electric field on the target rear. Clearly visible is the $2\omega_0$ imprinting of the laser frequency onto rear-side, promptly accelerated electrons. From comparisons between different deuterium ratios d, we find that an optimal absorption of laser energy into maximum number of electrons on the target rear ($y > 5.0\mu$m) and maximum accelerating field can be designed with about 20 - 50 % deuterium in the target. This leads to cutoff energy increase for $a_0 = 8 - 16$ of up to 18 % compared to a pure proton target of the same density.

Figure 8b) demonstrates that the target stays locally opaque even for $a_0 = 42$ during laser interaction: note the section at $y = 4 - 5\,\mu$m on which the electron density (red) is larger than the relativistic critical density (black). Nevertheless, plasma filaments are observed breaking up transverse sections of the target enabling burn-though.

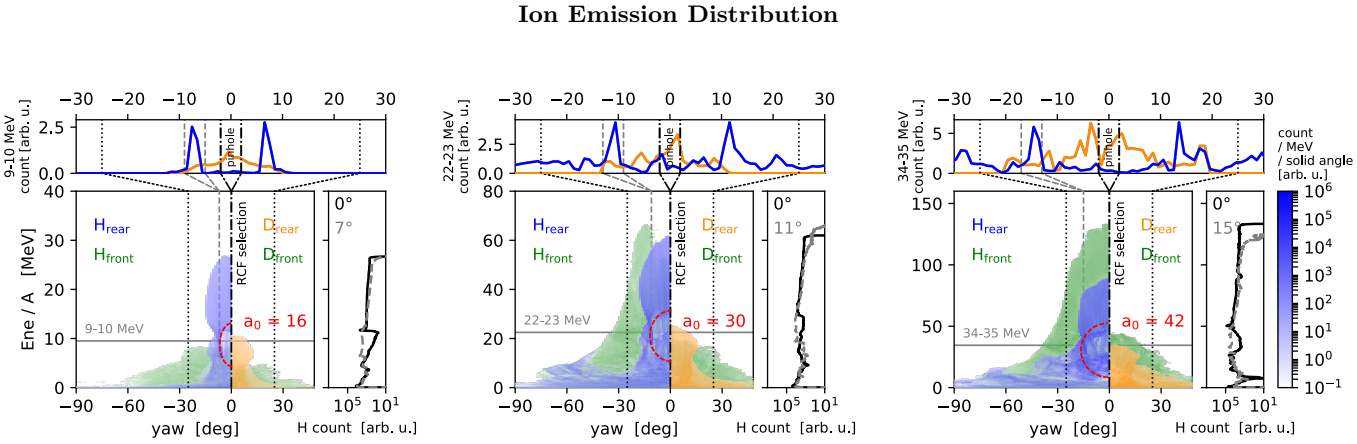

FIG. 9. **Lower plots:** Emission distribution of ions. Plotted for laser intensities $a_0 = 16, 30, 42$ (left-right) and target deuterium ratio $d = 90\%$. Left half is hydrogen (blue) and right half deuterium ions (orange) with green denoting front-originating ions in both cases. For large enough angle to the laser axis and energy, one can infer that only front-side ions contribute (areas plotted solely in green). Rear-side ions are plotted on top of front-side ions. **Upper plots:** A sample lineout, zoomed into a forward direction, shows emission characteristics for a selected energy ($\mathrm{d}E = 1\,$MeV), similar to an RCF layer (summed over front and rear contributions). **Side plots on right:** Energy lineout for pointing sensitivity with a pinhole aperture taken for acceptance on axis (black line: $(0 \pm 2)\,^\circ$) and off-axis (grey line: $(7, 11, 15 \pm 2)\,^\circ$), similar to a typical Thomson parabola.

Figure 9 shows the angular energy emission distribution in polarization direction. When comparing ion pointing for varying laser intensities, both hydrogen and deuterium emission distributions are more directed for low a_0 than higher

a_0. In our setup, front-side protons add a diffuse emission signature on top of the rear-side, directed protons due to hole-boring RPA contributions. The emission characteristics of hole-boring pre-accelerated ions from the target front surface (e.g. wider or narrower than the TNSA rear and structuring) depends on the given laser contrast and target pre-expansion and requires a detailed parameter scan for a given experiment. In our specific setup, front-side contributions emit into wider angles than rear-side ions. Note that the absolute values for energy and emission angle will both be smaller in 3D3V simulations and experiments, an experimental identification for areas of pure front-side contributions might be possible when clear structural changes are visible.

With increasing deuterium content in the target, the visible "hole" (marked red in Figure 9) in mid-range protons shifts to higher energies as more deuterium ions can displace the decreasing number of protons more efficiently. Experiments will observe a "gap" at low energies and quasi-monoenergetic features when observing strictly along the target normal with narrow angle acceptance. Under limited cryogenic target orientation stability[37] such measurements might suffer from shot-to-shot fluctuation of target normal alignment with respect to the fixed diagnostic axis. The lineouts on the right side of each plot in Figure 9 exemplify, how a positioning jitter of 7 ° ($a_0 = 16$), influences the measured spectra. Experimental campaigns can mitigate this issue by either collecting enough statistics or deploying wider, angle-resolved spectrometers (resolution $\leq 10\,°$).

In-Target Origin of Energetic Ions

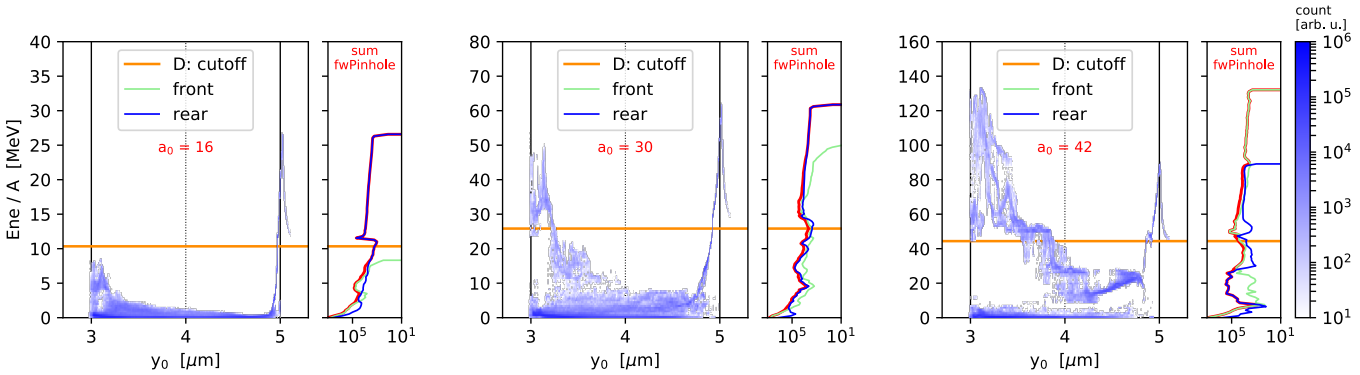

FIG. 10. Correlation of final energy depending on initial longitudinal position y_0 inside the target for hydrogen ions. Plotted for laser intensities $a_0 = 16, 30, 42$ and target deuterium ratio $d = 90\%$. y_0 describes the target along the laser-axis (laser from left), target front and rear are defined as initial position y_0 before or after 4 µm. Lines on the right show individual contributions of front (first micron up to $y_0 = 4$ in the target) and rear ions on the observed energy spectra in "forward pinhole" acceptance.

For TNSA, the highest accelerating fields are expected at the rear surface of the target. Figure 10 connects the initial target depth of a hydrogen ion with its finally reached energy. On the right of each figure, the forward-observed proton spectrum (red) with a blue line showing rear and green line showing front side contributions corresponds to the integral over the initial target depth.

Over increased a_0, the influence of front-side originating ions onto spectral modulations increases and finally dominates the cutoff energy for the PW-scale $a_0 = 42$. Front-side ions are further accelerated in the rear electro-static fields, which unsurprisingly leads to a similar spectral shape.

For an investigated a_0 of 30 and above, a deuterium ratio of 90 % is required to cause a significant modulation in the proton spectra. Accelerating rear fields scale with laser strengths from increased sheath electron energy. However, the superimposed multi-species fields that cause the spectral modulation do not increase with a_0 and depend on target composition.

Not only rear-surface protons experience a modulation, but also front-side hole-boring RPA protons are influenced by deuterium ions[13]. Further details are shown in Figure 11.

For $a_0 \gtrsim 30$, at energies in the spectrum above the cutoff of rear-side ions, one might expect a change in slope in the overall proton spectra as front side ions start to dominate the highest energies (red line in Figure 10). In some cases, a small energy modulation hints the change between the front and rear contributions which might not be significantly observable, since front-side ions are also pre-dominantly further accelerated in TNSA fields. As this is the observable obtained in an experiment, it is not possible to quickly infer which part of the spectrum is front- or rear-side originated without further radial emission information.

Multi-Species Effect on Front-Side Ions for $a_0 = 42$

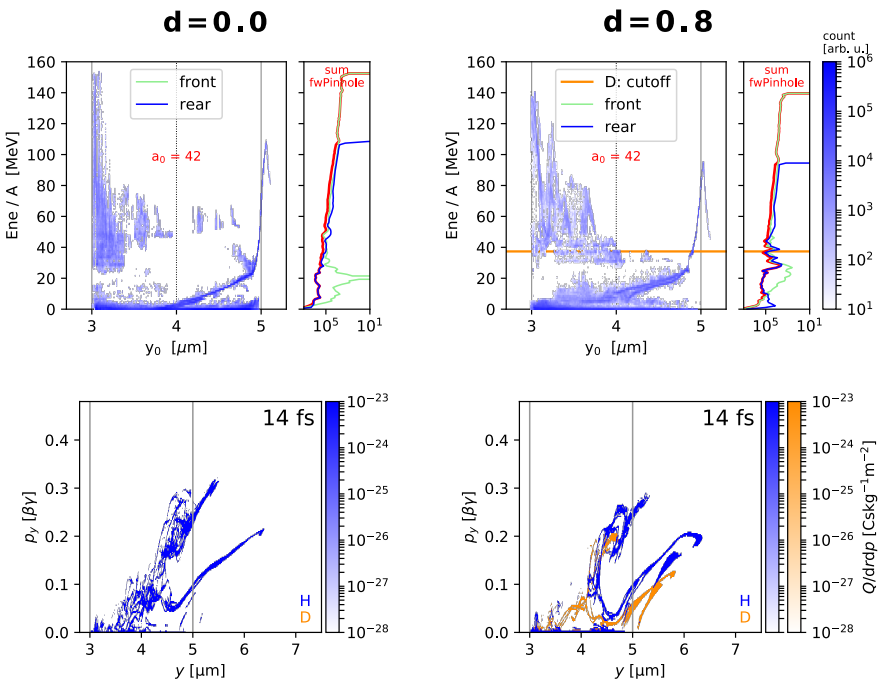

FIG. 11. Multi-species effect for front-side ions for $a_0 = 42$, comparing a pure hydrogen target ($d = 0.0$, left column) and a mixed target ($d = 0.80$, right column). Selected plots show particles in acceptance for a "forward pinhole". (Upper plots) Origin of final energies for hydrogen ions. (Lower plots) Longitudinal phase space for early times, 14 fs after laser peak intensity on target.

Figure 11 (top) shows a correlation plot between original in-target position and final energy of hydrogen ions for case $a_0 = 42$. For the high-deuterium case $d = 0.8$, front-side originating ions are equally affected by the multi-species effect from deuterium (see orange line for deuterium cutoff energy). The reason for that lies in the sufficiently long co-propagation through the target after initial front-side hole-boring acceleration. The longitudinal phase-space plots (bottom) show once again the proximity of deuterium and hydrogen ions as they are still within the target during burn-through, 14 fs after peak laser intensity on target.

Notes for Potential Experimental Realizations

For significant energy modulation signatures in the high-energy tail of distributions, a deuterium ratio $\geq 60\,\%$ is advisable. The observed multi-species effects are rather robust against small changes in deuterium ratio. Therefore, the mixing ratio only needs to be generated with a precision of few percent. Additionally, we observed a increase of proton cutoff energies in simulations for mixing ratios between 20 - 50 %.

For spectrometer setups, an energy resolution for the mid-energy range needs to be chosen that can resolve the few-MeV wide energy modulation. When deciding for an ion spectrometer with high energy resolution but small angular acceptance such as a Thomson parabola, a statistically significant amount of shots needs to be accumulated in case the target orientation jitter obfuscates the otherwise clear signature in the energy spectrum of target normal directed protons. The dynamic range in terms of proton counts per energy and solid angle should at least be three orders of magnitude for a good resolution of the start and end of the modulation.

* a.huebl@hzdr.de

[1] J. Fuchs, P. Antici, E. D'Humières, E. Lefebvre, M. Borghesi, E. Brambrink, C. A. Cecchetti, M. Kaluza, V. Malka, M. Manclossi, S. Meyroneinc, P. Mora, J. Schreiber, T. Toncian, H. Pépin, and P. Audebert, Nature Physics (2006), 10.1038/nphys199.

[2] S. C. Wilks, A. B. Langdon, T. E. Cowan, M. Roth, M. Singh, S. Hatchett, M. H. Key, D. Pennington, A. MacKinnon, and R. A. Snavely, Physics of Plasmas (2001), 10.1063/1.1333697.

[3] K. Zeil, S. D. Kraft, S. Bock, M. Bussmann, T. E. Cowan, T. Kluge, J. Metzkes, T. Richter, R. Sauerbrey, and U. Schramm, New J. Phys. **12**, 45015 (2010).

[4] A. V. Gurevich, L. V. Pariiskaya, and L. P. Pitaevskii, JETP **36**, 274 (1973).

[5] J. Denavit, Physics of Fluids (1979), 10.1063/1.862751.

[6] P. Mora, Physical Review Letters (2003), 10.1103/PhysRevLett.90.185002.

[7] K. Zeil, J. Metzkes, T. Kluge, T. Cowan, s. Kraft, and R. sauerbrey, Nature Communications **3** (2012), 10.1038/ncomms1883.

[8] T. Kluge, T. Cowan, A. Debus, U. Schramm, K. Zeil, and M. Bussmann, Physical Review Letters (2011), 10.1103/PhysRevLett.107.205003.

[9] T. Ditmire, J. W. G. Tisch, E. Springate, M. B. Mason, N. Hay, R. A. Smith, J. Marangos, and M. H. R. Hutchinson, Nature **386**, 54 (1997).

[10] M. Hegelich, S. Karsch, G. Pretzler, D. Habs, K. Witte, W. Guenther, M. Allen, A. Blazevic, J. Fuchs, J. C. Gauthier, M. Geissel, P. Audebert, T. Cowan, and M. Roth, Physical Review Letters (2002), 10.1103/PhysRevLett.89.085002.

[11] A. P. Robinson, A. R. Bell, and R. J. Kingham, Physical Review Letters (2006), 10.1103/PhysRevLett.96.035005.

[12] S. Steinke, P. Hilz, M. Schnürer, G. Priebe, J. Bränzel, F. Abicht, D. Kiefer, C. Kreuzer, T. Ostermayr, J. Schreiber, A. A. Andreev, T. P. Yu, A. Pukhov, and W. Sandner, Physical Review Special Topics - Accelerators and Beams (2013), 10.1103/PhysRevSTAB.16.011303.

[13] S. Kar, K. F. Kakolee, B. Qiao, A. MacChi, M. Cerchez, D. Doria, M. Geissler, P. McKenna, D. Neely, J. Osterholz, R. Prasad, K. Quinn, B. Ramakrishna, G. Sarri, O. Willi, X. Y. Yuan, M. Zepf, and M. Borghesi, Physical Review Letters (2012), 10.1103/PhysRevLett.109.185006.

[14] T. Sokollik, M. Schnürer, S. Ter-Avetisyan, P. V. Nickles, E. Risse, M. Kalashnikov, W. Sandner, G. Priebe, M. Amin, T. Toncian, O. Willi, and A. A. Andreev, Applied Physics Letters (2008), 10.1063/1.2890057.

[15] K. Quinn, P. A. Wilson, C. A. Cecchetti, B. Ramakrishna, L. Romagnani, G. Sarri, L. Lancia, J. Fuchs, A. Pipahl, T. Toncian, O. Willi, R. J. Clarke, D. Neely, M. Notley, P. Gallegos, D. C. Carroll, M. N. Quinn, X. H. Yuan, P. McKenna, T. V. Liseykina, A. MacChi, and M. Borghesi, Physical Review Letters (2009), 10.1103/PhysRevLett.102.194801.

[16] U. Masood, M. Bussmann, T. E. Cowan, W. Enghardt, L. Karsch, F. Kroll, U. Schramm, and J. Pawelke, Applied Physics B: Lasers and Optics (2014), 10.1007/s00340-014-5796-z.

[17] A. Macchi, S. Veghini, and F. Pegoraro, Physical Review Letters **103**, 85003 (2009).

[18] A. Macchi, M. Borghesi, and M. Passoni, Reviews of Modern Physics (2013).

[19] B. Qiao, S. Kar, M. Geissler, P. Gibbon, M. Zepf, and M. Borghesi, Physical Review Letters (2012), 10.1103/PhysRevLett.108.115002.

[20] Bulanov S V, Esirkepov T Zh, Kamenets F F, Kato Y, Kuznetsov A V, Nishihara K, Pegoraro F, Tajima T, and Khoroshkov V S, Plasma Physics Reports **28**, 975 (2002).

[21] T. Esirkepov, S. V. Bulanov, K. Nishihara, T. Tajima, F. Pegoraro, V. S. Khoroshkov, K. Mima, H. Daido, Y. Kato, Y. Kitagawa, K. Nagai, and S. Sakabe, Physical Review Letters (2002), 10.1103/PhysRevLett.89.175003, arXiv:0211104v1 [physics].

[22] S. M. Pfotenhauer, O. Jäckel, A. Sachtleben, J. Polz, W. Ziegler, H. P. Schlenvoigt, K. U. Amthor, M. C. Kaluza, K. W. Ledingham, R. Sauerbrey, P. Gibbon, A. P. Robinson, and H. Schwoerer, New Journal of Physics (2008), 10.1088/1367-2630/10/3/033034.

[23] K. Zeil, J. Metzkes, T. Kluge, M. Bussmann, T. E. Cowan, S. D. Kraft, R. Sauerbrey, B. Schmidt, M. Zier, and U. Schramm, Plasma Physics and Controlled Fusion **56**, 084004 (2014).

[24] C. Joshi, M. C. Richardson, and G. D. Enright, Applied Physics Letters (1979), 10.1063/1.90640.

[25] F. Begay and D. W. Forslund, Physics of Fluids (1982), 10.1063/1.863926.

[26] M. Allen, Y. Sentoku, P. Audebert, A. Blazevic, T. Cowan, J. Fuchs, J. C. Gauthier, M. Geissel, M. Hegelich, S. Karsch, E. Morse, P. K. Patel, and M. Roth, Physics of Plasmas (2003), 10.1063/1.1592154.

[27] A. J. Kemp and H. Ruhl, Physics of Plasmas (2005), 10.1063/1.1856933.

[28] J. Psikal, V. T. Tikhonchuk, J. Limpouch, A. A. Andreev, and A. V. Brantov, Physics of Plasmas (2008), 10.1063/1.2913264.

[29] V. T. Tikhonchuk, A. A. Andreev, S. G. Bochkarev, and V. Y. Bychenkov, in Plasma Physics and Controlled Fusion (2005).

[30] T. Kluge, W. Enghardt, S. D. Kraft, U. Schramm, K. Zeil, T. E. Cowan, and M. Bussmann, Phys. Plasmas **17**, 123103 (2010).

[31] P. Hilz, T. M. Ostermayr, A. Huebl, V. Bagnoud, B. Borm, M. Bussmann, M. Gallei, J. Gebhard, D. Haffa, J. Hartmann, T. Kluge, F. H. Lindner, P. Neumayr, C. G. Schaefer, U. Schramm, P. G. Thirolf, T. F. Rösch, F. Wagner, B. Zielbauer, and J. Schreiber, Nature Communications (2018), 10.1038/s41467-017-02663-1.

[32] A. V. Brantov, V. T. Tikhonchuk, O. Klimo, D. V. Romanov, S. Ter-Avetisyan, M. Schnürer, T. Sokollik, and P. V. Nickles, Physics of Plasmas (2006), 10.1063/1.2404928.

[33] S. Garcia, D. Chatain, and J. P. Perin, Laser and Particle Beams (2014), 10.1017/S0263034614000524.

[34] D. Margarone, A. Velyhan, J. Dostal, J. Ullschmied, J. P. Perin, D. Chatain, S. Garcia, P. Bonnay, T. Pisarczyk, R. Dudzak, M. Rosinski, J. Krasa, L. Giuffrida, J. Prokupek, V. Scuderi, J. Psikal, M. Kucharik, M. De Marco, J. Cikhardt, E. Krousky, Z. Kalinowska, T. Chodukowski, G. A. Cirrone, and G. Korn, Physical Review X (2016), 10.1103/PhysRevX.6.041030.

[35] S. Göde, C. Rödel, K. Zeil, R. Mishra, M. Gauthier, F. E. Brack, T. Kluge, M. J. Macdonald, J. Metzkes, L. Obst, M. Rehwald, C. Ruyer, H. P. Schlenvoigt, W. Schumaker, P. Sommer, T. E. Cowan, U. Schramm, S. Glenzer, and F. Fiuza, Physical Review Letters (2017), 10.1103/PhysRevLett.118.194801.

[36] S. D. Kraft, L. Obst, J. Metzkes-Ng, H. P. Schlenvoigt, K. Zeil, S. Michaux, D. Chatain, J. P. Perin, S. N. Chen, J. Fuchs, M. Gauthier, T. E. Cowan, and U. Schramm, Plasma Physics and Controlled Fusion (2018), 10.1088/1361-6587/aaae38.

[37] L. Obst, S. Göde, M. Rehwald, F. E. Brack, J. Branco, S. Bock, M. Bussmann, T. E. Cowan, C. B. Curry, F. Fiuza, M. Gauthier, R. Gebhardt, U. Helbig, A. Huebl, U. Hübner, A. Irman, L. Kazak, J. B. Kim, T. Kluge, S. Kraft, M. Loeser, J. Metzkes, R. Mishra, C. Rödel, H. P. Schlenvoigt, M. Siebold, J. Tiggesbäumker, S. Wolter, T. Ziegler, U. Schramm, S. H. Glenzer, and K. Zeil, Scientific Reports (2017), 10.1038/s41598-017-10589-3.

[38] L. Obst-Huebl, T. Ziegler, F.-E. Brack, J. Branco, M. Bussmann, T. E. Cowan, C. B. Curry, F. Fiuza, M. Garten, M. Gauthier, S. Göde, S. H. Glenzer, A. Huebl, A. Irman, J. B. Kim, T. Kluge, S. D. Kraft, F. Kroll, J. Metzkes-Ng, R. Pausch, I. Prencipe, M. Rehwald, C. Roedel, H.-P. Schlenvoigt, U. Schramm, and K. Zeil, Nature Communications **9** (2018), 10.1038/s41467-018-07756-z.

[39] G. G. Scott, D. C. Carroll, S. Astbury, R. J. Clarke, C. Hernandez-Gomez, M. King, A. Alejo, I. Y. Arteaga, R. J. Dance, A. Higginson, S. Hook, G. Liao, H. Liu, S. R. Mirfayzi, D. R. Rusby, M. P. Selwood, C. Spindloe, M. K. Tolley, F. Wagner, E. Zemaityte, M. Borghesi, S. Kar, Y. Li, M. Roth, P. McKenna, and D. Neely, Phys. Rev. Lett. **120**, 204801 (2018).

[40] J. B. Kim, C. Schoenwaelder, and S. H. Glenzer, Review of Scientific Instruments (2018), 10.1063/1.5038561.

[41] The screening length corresponds to the classical Debye length in a thermalized plasma. We checked the validity of our assumption in our PIC simulations. E.g., for $a_0 = 16$ and medium deuterium concentration of $d = 0.5$, the screening length at the de-mixed ion front was measured to be increasingly larger than $0.5\,\mu\text{m}$ while the distance between the ion fronts was below $1.0\,\mu\text{m}$ up to $t^{\text{peak}} \approx 1.7\,\tau_{\text{laser}}$.

[42] J. E. Allen and J. G. Andrews, Journal of Plasma Physics (1970), 10.1017/S0022377800004906.

[43] M. Bussmann, H. Burau, T. E. Cowan, A. Debus, A. Huebl, G. Juckeland, T. Kluge, W. E. Nagel, R. Pausch, F. Schmitt, U. Schramm, J. Schuchart, and R. Widera (2013).

[44] A. Huebl, R. Widera, B. Worpitz, R. Pausch, H. Burau, M. Garten, S. Starke, A. Grund, A. Debus, A. Matthes, S. Bastrakov, K. Steiniger, I. Göthel, S. Rudat, J. Kelling, and M. Bussmann, "PIConGPU 0.4.3: System Updates and Bug Fixes," (2019).

[45] U. Schramm, M. Bussmann, A. Irman, M. Siebold, K. Zeil, D. Albach, C. Bernert, S. Bock, F. Brack, J. Branco, J. P. Couperus, T. E. Cowan, A. Debus, C. Eisenmann, M. Garten, R. Gebhardt, S. Grams, U. Helbig, A. Huebl, T. Kluge, A. Köhler, J. M. Krämer, S. Kraft, F. Kroll, M. Kuntzsch, U. Lehnert, M. Loeser, J. Metzkes, P. Michel, L. Obst, R. Pausch, M. Rehwald, R. Sauerbrey, H. P. Schlenvoigt, K. Steiniger, and O. Zarini, in Journal of Physics: Conference Series (2017).

[46] A. P. Robinson, P. Gibbon, M. Zepf, S. Kar, R. G. Evans, and C. Bellei, Plasma Physics and Controlled Fusion (2009), 10.1088/0741-3335/51/2/024004.

[47] J. Schreiber, F. Bell, F. Grüner, U. Schramm, M. Geissler, M. Schnürer, S. Ter-Avetisyan, B. M. Hegelich, J. Cobble, E. Brambrink, J. Fuchs, P. Audebert, and D. Habs, Physical Review Letters (2006), 10.1103/PhysRevLett.97.045005.